# Finite element modeling of short-wavelength folding on Venus: Implications for the plume hypothesis for crustal plateau formation

Rebecca R. Ghent
Center for Earth and Planetary Studies, Smithsonian Institution, Washington, D. C., USA

Roger J. Phillips
Department of Earth and Planetary Sciences, Washington University, St. Louis, Missouri, USA

Vicki L. Hansen
Department of Geological Sciences, University of Minnesota, Duluth, Minnesota, USA

Daniel C. Nunes
Lunar and Planetary Institute, Houston, Texas, USA

Received 29 June 2005; revised 6 September 2005; accepted 19 September 2005; published 26 November 2005.

[1] The key geological observations and structural interpretations associated with the current plume hypothesis for Venusian crustal plateau formation are that (1) short-wavelength, spatially periodic tectonic structures originated as mechanical instabilities in a regionally extensive surface brittle layer whose basal boundary was thermally generated and controlled; (2) characteristic wavelengths of spatially periodic structures record the brittle layer thickness at the time of deformation; and (3) structural wavelengths increased with time, driven by brittle layer thickening in response to cooling. The plume hypothesis accommodates these constraints by proposing that crustal plateaus formed above mantle plumes impinging on thin lithosphere; it further suggests that surface temperatures temporarily elevated to ~1000 K may have been required to maintain a sufficiently thin brittle layer for formation of the shortest-wavelength structures. We report here on finite element simulations designed to test the feasibility of the proposed thermal conditions. Specifically, we model formation of short-wavelength folds thought to have initiated as contractional layer instabilities early in the plateau formation process. Under high surface temperatures, the finite element meshes develop semibrittle zones in which short-wavelength folds can form, but development of even modest structural relief requires unrealistically high total mesh shortening. Thus elevated surface temperatures inhibit development of short-wavelength folds because the models' effective integrated mechanical strength under such hot conditions is excessively low. Decreasing the surface temperature increases structural relief but produces tectonic wavelengths that are larger than those observed. We conclude that a model with solely thermal control of mechanical properties cannot explain the observed structures.

**Citation:** Ghent, R. R., R. J. Phillips, V. L. Hansen, and D. C. Nunes (2005), Finite element modeling of short-wavelength folding on Venus: Implications for the plume hypothesis for crustal plateau formation, *J. Geophys. Res.*, *110*, E11006, doi:10.1029/2005JE002522.

## 1. Introduction

[2] Crustal plateaus preserve some of Venus' oldest observed and most extensive structural deformation. If crustal plateau deformation is genetically linked to formation of the plateaus themselves, as has been proposed previously [e.g., *Bindschadler et al.*, 1992a, 1992b; *Bindschadler*, 1995; *Hansen et al.*, 1997, 1999, 2000; *Gilmore et al.*, 1998; *Ghent and Hansen*, 1999], then the structures preserved in crustal plateaus can provide important insights into Venus' geological history. Competing geodynamical models make fundamentally different predictions for the formation mechanisms of tessera terrain; thus the sequence and mechanisms of deformation recorded in tessera terrain may have profound implications for the history of Venus. In this paper, we report on finite element simulations of structural deformation related to crustal plateau formation and use the results to evaluate the validity of the plume hypothesis for crustal plateau origin. This hypothesis was originally formulated largely on geodynamical arguments [*Herrick and Phillips*, 1990; *Phillips et al.*, 1991; *Smrekar and Phillips*, 1991]. After high-resolution radar images became available from the Magellan mission,


0148-0227/05/2005JE002522$09.00

it was refined to accommodate structural and kinematic characteristics of the distinctive tectonic features observed on crustal plateaus [*Phillips and Hansen*, 1994, 1998; *Hansen and Willis*, 1998]. Specifically, the plume mechanism as presented by *Phillips and Hansen* [1998] advocates a unique set of thermal and mechanical conditions, but the local lithospheric response to these conditions has not been explored in detail.

[3] The purpose of the current work is to evaluate the physical and geological plausibility of one key prediction of the plume hypothesis, specifically, that mechanical instabilities can arise in a brittle layer whose thickness is solely thermally controlled, and that these instabilities can ultimately lead to formation of spatially periodic tectonic structures. We employ the conditions proposed in the plume hypothesis as presented by *Hansen and Willis* [1998], *Phillips and Hansen* [1998], and *Hansen et al.* [1999, 2000]; namely, we use a compositionally uniform crust with temperature-dependent rheology that is allowed to cool from its initially hot state (specifically, using elevated surface temperatures up to 1000 K, representing the early stages of crustal plateau deformation as envisioned in the plume hypothesis) while being subjected to tectonic forces. The goal is to determine whether a brittle-ductile transition (BDT) arises in such a model, and whether the wavelengths of any tectonic structures that form are controlled by the depth or motion of this boundary during the model evolution.

[4] The modeling presented here uses an elastoviscoplastic (EVP) rheology, which allows simulation of three simultaneous deformation mechanisms at every location in a finite element mesh. The dominant deformation mechanism(s) at any location is governed by local mechanical and thermal conditions and can evolve in response to changing conditions. This allows for a more flexible and adaptable representation of rock deformation than is possible in simulations for which the rheology of each model element is determined a priori (e.g., models with predefined compositional or mechanical layering). This approach is well suited to the problem at hand because it allows us to explore the prediction of the plume hypothesis that important rheological boundaries arise in response to solely thermal drivers.

[5] In this paper, we first review the fundamental characteristics of crustal plateaus and their distinctive structural fabrics, and outline the observations and interpretations that have led to the tectonic predictions of the current plume hypothesis. We then present the details of our finite element simulations and discuss the ways in which these simulations can be used to test the feasibility of the plume hypothesis. Finally, we outline our model results and discuss their implications for the mechanisms of crustal plateau formation.

## 2. Background: Tessera Terrain and Models for Crustal Plateau Formation

[6] Venus' crustal plateaus are roughly circular features, 1000–2500 kilometers in diameter and 2–4 kilometers above mean planetary radius, that are characterized by pervasive "tessera" deformation [*Barsukov et al.*, 1986; *Basilevsky et al.*, 1986]. The processes of tessera formation and their relationship to crustal plateaus have been explored in an extensive body of work [e.g., *Head and Crumpler*, 1987; *Herrick and Phillips*, 1990; *Bindschadler and Head*, 1991; *Bindschadler et al.*, 1992a, 1992b; *Bindschadler*, 1995; *Grimm*, 1994; *Brown and Grimm*, 1997; *Hansen and Willis*, 1996, 1998; *Ivanov and Head*, 1996; *Pritchard et al.*, 1997; *Gilmore et al.*, 1997, 1998; *Head and Basilevsky*, 1998; *Phillips and Hansen*, 1994, 1998; *Hansen et al.*, 1997, 1999, 2000; *Ghent and Hansen*, 1999; *Banks and Hansen*, 2000]. The structural pattern that characterizes crustal plateau tessera (Figure 1) consists of: a pervasive, closely spaced, quasiperiodic extensional fabric defined by long (tens to 100 km), narrow (1–5 km), shallow (hundreds of m) troughs bounded by tensile or shear fractures (dubbed "ribbons" by *Hansen and Willis* [1996]); a spatially overlapping fold fabric; and a disorganized pattern of wide lensoidal complex graben that generally trend perpendicular to ridge crests. At the plateau margins, the fold fabric is commonly organized into long, wide, margin-parallel belts perpendicular to the trend of the pervasive extensional fabric [e.g., *Bindschadler et al.*, 1992a, 1992b; *Brown and Grimm*, 1997; *Gilmore et al.*, 1997, 1998; *Ghent and Hansen*, 1999]. This fold fabric shows a wide range of crest spacings (hundreds of meters to >30 km). In some plateau interiors, the folds comprise a disorganized, basin-and-dome type terrain.

### 2.1. Sequence of Deformation and the Plume Hypothesis

[7] Inferred timing relationships among these structural suites have been cited to support competing models for crustal plateau formation. For example, on the basis of an analysis of the structures at Alpha Regio, *Bindschadler et al.* [1992b] interpreted folding as the earliest stage of deformation, and all of the extensional features as younger. From these kinematic interpretations, *Bindschadler et al.* [1992a, 1992b] proposed a "coldspot" hypothesis, in which crustal plateaus form above long-lived convective or diapiric mantle downwellings, resulting in horizontal convergence of ductile lower crust driven by mechanical coupling between crust and mantle, and leading to crustal thickening. This model predicts a strain history of early, intense contraction, followed by late extension resulting from gravitational relaxation. *Gilmore et al.* [1998] also favored the coldspot hypothesis on the basis of their interpretations of tessera deformation sequences. The coldspot model has been criticized on the grounds that plateau-like crustal thickening of dry diabase (commonly used as an analog for Venusian crust [*Mackwell et al.*, 1998]) by subsolidus flow would require a geologically unreasonable length of time [*Kidder and Phillips*, 1996], and on the basis of other geophysical criteria [*Phillips and Hansen*, 1994; *Hansen et al.*, 1997].

[8] *Pritchard et al.* [1997], *Hansen and Willis* [1996, 1998], and *Ghent and Hansen* [1999] arrived at a different conclusion based on their structural and kinematic analyses of crustal plateau deformation patterns, and argued that ribbon structures predate the long-wavelength folds and complex lensoidal graben on the basis of mechanical factors. This led to a reinvigoration of the plume model, originally motivated by geodynamic considerations. Clear cross-cutting relationships among ribbons and folds are rare,

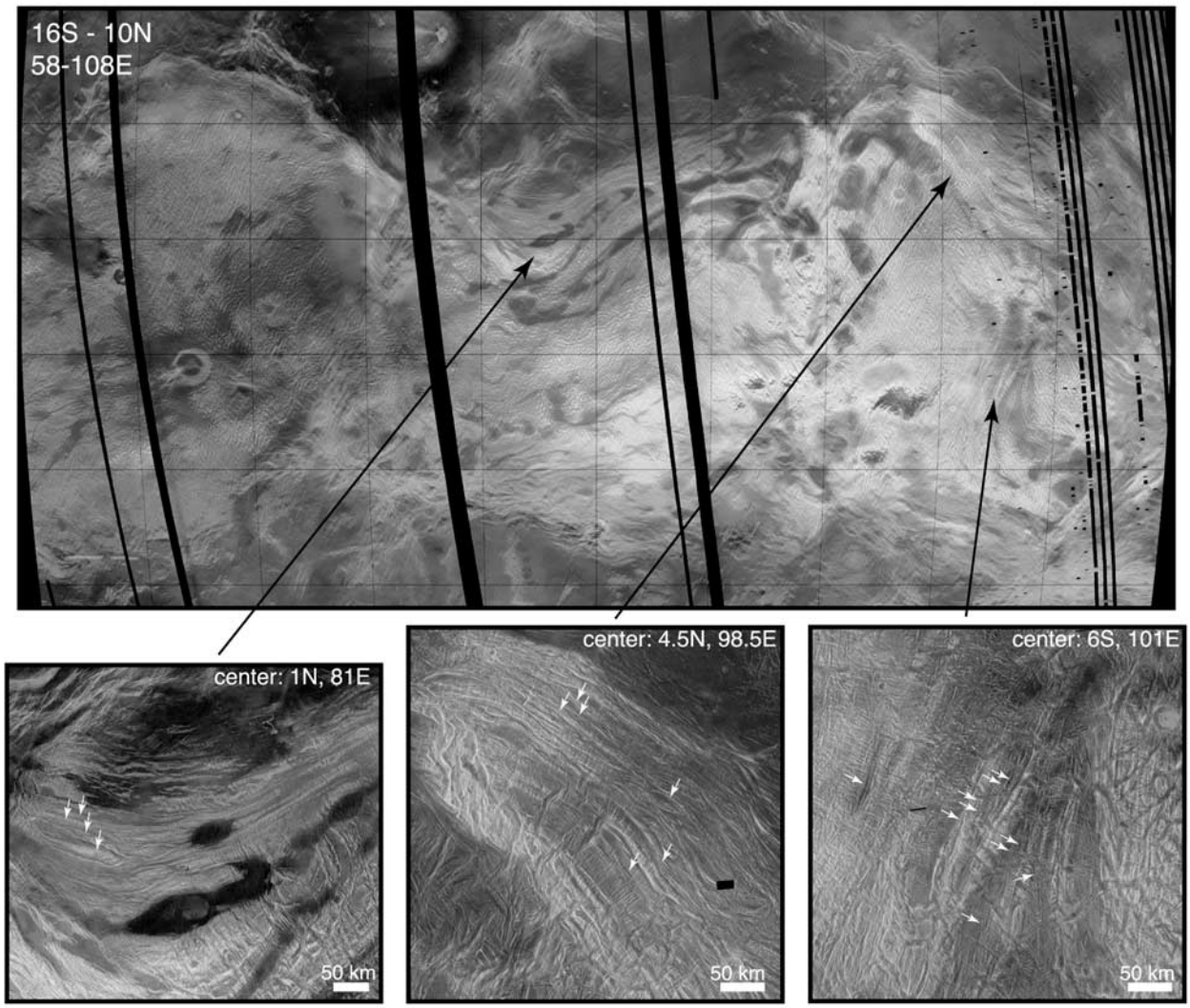


**Figure 1.** (top) Magellan SAR image of Ovda Regio showing (bottom) geographic locations of full-resolution detail images. White arrows in detail images indicate a few of the regions containing folds of wavelength 1 km or less; close examination of digital full-resolution images reveals that these folds occur down to the resolution of the SAR images in some regions.

though some have been documented [*Banks and Hansen*, 2000]. Unique age relationships for ribbons relative to spatially overlapping folds are difficult to establish [*Ghent and Hansen*, 1999; *Hansen et al.*, 2000]. In order to do so, *Ghent and Hansen* [1999] turned to mechanical arguments. Because ribbons and large folds exhibit two distinct scales of deformation, the two structural suites record different mechanical layer thicknesses. Ribbon fabric is a quasiperiodic fabric with a small (1–5 km) characteristic wavelength, and hence arises from deformation of a layer of smaller effective mechanical thickness than the longer-wavelength (5 to >30 km) folds [*Hansen and Willis*, 1996, 1998; *Phillips and Hansen*, 1998; *Ghent and Hansen*, 1999]. Because the two structural suites are spatially correlative and share the same principal strain orientations, they could represent phases in a progressive deformation, with layer thickness as the evolving parameter [*Ghent and Hansen*, 1999]. *Hansen and Willis* [1996, 1998], *Phillips and Hansen* [1998] and *Ghent and Hansen* [1999] argued that it was most geologically plausible for ribbons to have formed first, in a thermally thinned lithosphere over a hot plume, and for the long-wavelength folds to have come later, when lithospheric cooling driven by waning of the plume strength would have thickened the deforming layer. The final stage of deformation would involve localized extension of high topography, resulting in short, wide, lensoidal graben cutting high long-wavelength fold crests.

[9] This inferred sequence led to a key idea: that each crustal plateau surface must have been healed of preexisting structures and mechanical fabrics on essentially all macroscopic scales prior to the first recorded phase of deformation, allowing ribbon terrain formation by extension of a thin, mechanically uniform surface layer overlying a weak substrate [*Hansen and Willis*, 1998]. The apparent absence of a second spatially periodic extensional fabric with a longer characteristic wavelength was thought to favor

formation of ribbon terrain by extension of a single mechanical layer rather than a rheologically layered package of rocks such as that found in the Basin and Range province [e.g., *Fletcher and Hallet*, 1983; *Zuber and Parmentier*, 1996]. On the basis of well-known relationships between structural wavelengths and mechanical layer thickness for single-layer extension, *Hansen and Willis* [1998], *Ghent and Hansen* [1999], and *Ghent and Tibuleac* [2002] suggested that ribbons likely formed in a brittle layer less than ~3 kilometers thick (and in fact, on the order of hundreds of meters for some ribbons). These authors further proposed that the depth of the base of this layer was thermally controlled, and that it in fact represented the regional BDT. The initial stages of crustal plateau deformation were proposed to occur as the crust cooled from an initially hot state caused by volcanic resurfacing and/or magmatic intrusions, which would erase previous structures and produce a mechanically uniform crust. With cooling, the BDT would migrate downward from the surface, and local and regional tectonic stresses would favor formation of the observed tectonic structures. Under this scheme, the characteristic wavelengths of the structures formed in the brittle layer would increase with the depth to the BDT.

[10] Lithospheric updoming resulting from the presence of a hot plume in the shallow mantle should result in tensional hoop stresses as well as radial compression near the edges of the uplift, leading to radially oriented extensional features and circumferential contractional features at the margins. For a thin deforming layer subjected to these stresses, short-wavelength structures of both extensional and contractional nature could develop and overlap spatially near the uplift margins if the local stresses are advantageously oriented. In the simplest case, in which the lithosphere is mechanically homogeneous and isotropic and in an isotropic stress field, ribbons could play the role of the radially oriented extensional features, and the margin-parallel fold belts are the circumferential contractional structures, as observed at Ovda Regio. In the presence of an additional, superposed regional stress field, the orientations of the contractional and extensional features could change, but the two suites should still be mutually perpendicular unless a mechanical anisotropy (e.g., a preexisting tectonic fabric) exists to disrupt the mechanical uniformity of the lithosphere.

### 2.2. Implications of a Shallow BDT

[11] For a reasonably sized thermal plume to produce a BDT as shallow as that proposed for ribbon formation, the overlying lithosphere would have to have been relatively thin, as has been proposed in some global evolution models [e.g., *Hansen and Willis*, 1998] (also see *Phillips and Hansen* [1998] for a discussion of the transition from thin- to stagnant-lid convection). The surface temperature imposes a stringent boundary condition on a cooling crustal column, and largely determines the rate of downward migration of the BDT [*Hansen et al.*, 2000]. In order to maintain a shallow BDT (within several hundred meters of the surface for the shortest-wavelength ribbons [*Hansen and Willis*, 1998]) for a sufficient length of time to allow ribbon terrain to develop at a reasonable rate, *Phillips and Hansen* [1998] suggested that the surface temperature during ribbon formation may have been elevated, perhaps to as much as 1000 K. *Phillips and Hansen* [1998], *Bullock and Grinspoon* [2001], and *Phillips et al.* [2001] proposed a possible mechanism for this, involving feedbacks between magmatic outgassing and atmospheric infrared opacity, during one or more episodes of volcanic resurfacing of the regional plains.

[12] If the characteristic wavelength of spatially periodic structures can be related in such a direct way to the instantaneous regional depth of the BDT, and if the plateaus cooled monotonically from a hot initial state, then the shortest characteristic wavelength must record the initial thermal conditions for a given plateau. The shortest-wavelength folds found in crustal plateaus show characteristic wavelengths on the order of hundreds of meters. Conservative estimates of the ratio of fold wavelength to layer thickness ($\lambda$/H) of 2–4 [e.g., *Biot*, 1961; *Sherwin and Chapple*, 1968; *Fletcher*, 1974; *Zuber and Parmentier*, 1996] yield estimates for the depth to the BDT on the order of 100 m for these structures. This is an even more stringent requirement than the depth proposed for ribbons, and should be possible only for a restricted range of physical parameters.

[13] In this paper, we focus on these short-wavelength folds, located near the plateau margins (Figure 1). Despite exhaustive discussions of ribbon terrain and long-wavelength folds, no systematic examination of the short-wavelength contractional features found in the crustal plateau fold belts has been conducted. We wish to determine whether or not formation of short-wavelength contractional features matching those observed is feasible under the conditions proposed in the plume hypothesis. Because ribbons and short-wavelength folds occur together at the margins of crustal plateaus and show compatible principal strain orientations [*Ghent and Hansen*, 1999], it is possible that they formed simultaneously, under the principle that the shortest-wavelength tectonic features represent the earliest stages of deformation. If that is the case, the conditions required to form one structural suite must also allow formation of the other. The salient point to be evaluated (that is, whether or not changes in the local thermal profile alone can generate sharp rheological discontinuities that would encourage growth of periodic mechanical instabilities) could be addressed using simulations of either folding or ribbon formation. We chose to treat folding in our simulations because folding can be modeled in a continuous medium without loss of cohesion; this is far easier to implement in a finite element simulation than formation of and motion along faults or fracture surfaces. As outlined in the following sections, the results provide insight into the physical and geological implications of the plume hypothesis. They also identify shortcomings and provide some avenues for further investigation.

## 3. Method

[14] We used the commercial software package MSC.MARC-Mentat (http://www.mscsoftware.com) to construct 2D finite element simulations of simultaneous cooling and horizontal shortening of the shallow Venusian crust. The "success criterion" was twofold: development of short-wavelength contractional topography with (1) maximum vertical relief of at least 10 m and (2) at least one

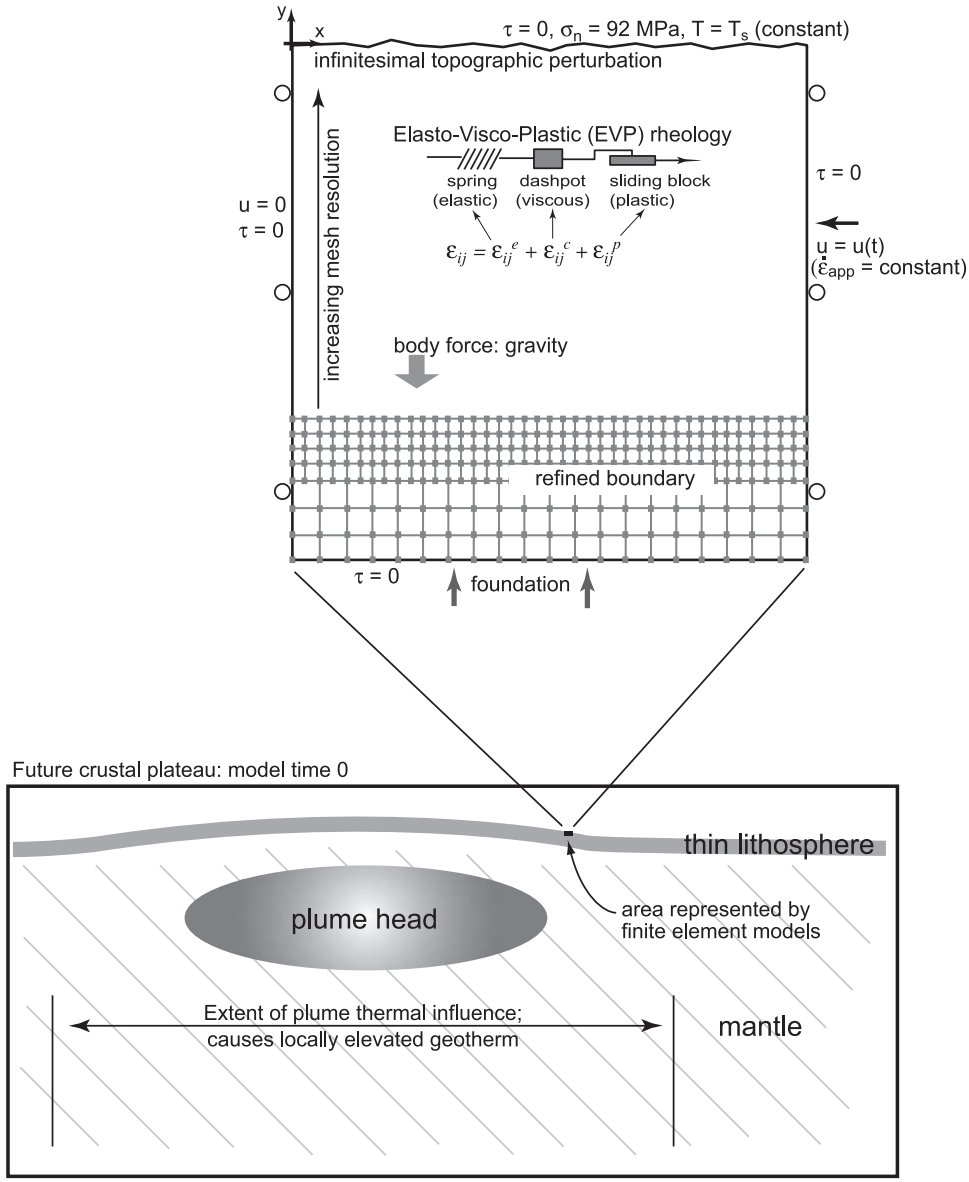


**Figure 2.** (bottom) Schematic diagram representing the geodynamical context for the finite element simulations (not to scale). (top) Schematic diagram illustrating the geometry and boundary conditions for a typical finite element mesh: $\tau$, shear stress; $\sigma_n$, normal stress; $u$, velocity; $\dot{\varepsilon}_{app}$, applied shortening rate; $\varepsilon_{ij}$, element of deviatoric strain tensor. The total strain in any element is the sum of elastic, creep, and plastic strain components.

characteristic topographic component with wavelength less than 1 km. These criteria were intentionally lenient to prevent discarding any viable results; in actuality, the real amplitudes of crustal plateau short-wavelength folds are likely on the order of 100 m [e.g., *Ghent and Hansen*, 1999]. Sensitivity to variations in thermal and mechanical parameters was tested in a series of 31 simulations. The advantage to using a finite element approach is that it allows use of an elastoviscoplastic (EVP) rheology, in which each element can select its own dominant deformation mode(s) in response to local conditions. Thus rheological boundaries (e.g., layering) need not be specified a priori, but can develop and evolve spontaneously in response to local drivers.

[15] MARC has been used previously to examine tectonic processes on various scales and on multiple planets [e.g., *Mancktelow*, 1999; *Albert and Phillips*, 2000, 2002; *Albert et al.*, 2000; *Brown and Phillips*, 2000; *Dombard and McKinnon*, 2000; *Dombard and Freed*, 2002; *Nunes et al.*, 2004]. The most relevant of these studies to the current work is that of *Mancktelow* [1999], in which viscoelastic finite element simulations constructed using MARC were used to examine the effects of initial perturbation geometry on wavelength selection in single layer folding. In that work, a relatively competent power law viscoelastic layer with fixed thickness was embedded in a weaker power law viscoelastic matrix and subjected to a constant strain rate layer-parallel compression. Unfortunately we cannot

**Table 1.** Model Constants

| Parameter | Symbol | Value |
|---|---|---|
| Young's modulus | E | $6 \times 10^{10}$ Pa |
| Poisson's ratio | $\nu$ | 0.25 |
| Angle of internal friction | $\phi$ | 30° |
| Gravitational acceleration | g | 8.87 m/s$^2$ |

directly compare our current work to that study, because we did not use layers with different rheological properties in our simulations, and we used an EVP rheology rather than a viscoelastic one.

[16] MARC solves the equations of mechanical equilibrium in conjunction with a constitutive relation relating stress to strain or strain rate via adopted rheological laws. The total strain in the EVP rheological model is defined as the sum of the elastic, creep, and plastic strains:

$$\varepsilon_{ij} = \varepsilon^e_{ij} + \varepsilon^c_{ij} + \varepsilon^p_{ij}. \tag{1}$$

Such a material can be represented by a Maxwell viscoelastic formulation extended to include plasticity, and can be thought of as the series addition of a linear elastic spring, a viscous dashpot, and a frictional sliding block (Figure 2) [e.g., *Albert et al.*, 2000]. Plastic strains occur when model stresses exceed the yield stress defined by the Drucker-Prager criterion, given by

$$\alpha I_1 + \sqrt{J_2} - \frac{\bar{\sigma}}{\sqrt{3}} = 0, \tag{2}$$

where $I_1$ is the first stress invariant, $J_2$ is the second invariant of the deviatoric stress, and $\bar{\sigma}$ is the mean stress. The constant $\alpha$ and the mean stress are related to the cohesion $c$ and angle of internal friction $\phi$ (derived from Byerlee's rule; value given in Table 1) by the expressions

$$c = \frac{\bar{\sigma}}{\sqrt{3(1 - 12\alpha^2)}} \tag{3}$$

and

$$\sin\phi = \frac{3\alpha}{\sqrt{(1 - 3\alpha^2)}}. \tag{4}$$

Plasticity as used here represents a time-independent inelastic deformation that includes frictional slip and brittle fracture in a continuum approximation. Our simulations can identify zones of brittle failure (as represented by a plastic continuum) but cannot treat formation of or slip along individual faults. It should be noted that this representation does not refer to crystal plastic mechanisms such as dislocation climb or glide, grain boundary sliding, or twinning; these mechanisms can be included in the various creep laws available in MARC to define viscous behavior. We will use the terms "plastic" or "brittle" to refer to the brittle components of strain in the simulations discussed in this paper, and the terms "creep" or "ductile" to refer to the viscous (specifically, steady state incompressible creep) components of the deformation.

[17] Elastic stresses occur instantaneously in the mesh with application of each load increment, and are relieved by incompressible steady state creep and plasticity. We use canonical values for elastic constants Poisson's ratio and Young's modulus $\nu$ and $E$ (e.g., *Turcotte and Schubert* [1982]; Table 1). MARC calculates an increment of creep strain $\Delta\varepsilon^c_E$ for each time step $\Delta t$ according to

$$\Delta\varepsilon^c_E = A\sigma^n_E e^{-Q/RT}\Delta t, \tag{5}$$

where the subscript $E$ denotes equivalent quantities (i.e., $\varepsilon^c_E \equiv \sqrt{{}^2\!/_3\varepsilon^c_{ij}\varepsilon^c_{ij}}$ and $\sigma_E \equiv \sqrt{{}^3\!/_2\sigma'_{ij}\sigma'_{ij}} = \sqrt{3J_2}$, where primes denote deviatoric quantities). The model creep behavior is governed by steady state flow laws determined in high-temperature creep experiments of anhydrous Columbia and Maryland diabase [*Mackwell et al.*, 1998]:

$$\text{Columbia diabase} \qquad \dot{\varepsilon} = 190\sigma^{4.7}\, e^{-485/RT}, \tag{6a}$$

$$\text{Maryland diabase} \qquad \dot{\varepsilon} = 8\sigma^{4.7}\, e^{-485/RT}, \tag{6b}$$

where strain rate ($\dot{\varepsilon}$) is in s$^{-1}$, deviatoric stress ($\sigma$) is in MPa, the activation energy ($Q$) is in kJ/mol, $R$ is the ideal gas constant, and temperature ($T$) is in K. The code uses an automatic time stepping method in which convergence is determined at each time step by user-specified tolerances on creep strain change relative to elastic strain, stress change relative to current stress, and the sum of residual forces relative to reaction forces. If all of the tolerances are met during the initial increment, the size of the time step is increased for the next increment. If any of the tolerances is exceeded, the increment is recycled using a smaller time step until the tolerances are met or until the maximum allowable number of iterations has occurred.

[18] Classical treatments of single-layer folding [e.g., *Biot*, 1961; *Ramberg*, 1962; *Fletcher*, 1974; *Smith*, 1977, 1979; *Zuber and Parmentier*, 1996] predict that initiation of mechanical instabilities should occur at relatively small total strains (within a few percent total shortening). In these treatments, growth of macroscopic structures proceeds fairly rapidly once they are initiated, and the growth rates are largely determined by the strength or competence contrast between the layer and the matrix, and require a boundary between the two layers across which the mechanical properties are discontinuous. Because our meshes did not have compositional or mechanical layering, and it was unknown at the outset whether sharp rheological discontinuities could arise from variations in thermal profile alone, it was unclear a priori whether these previous studies could provide much guidance concerning the geological time or degree of total shortening required for these instabilities to arise in the finite element meshes. We specified run times of 5–10 Myr depending on the applied shortening rates, with the expectation that tectonic structures should initiate and begin amplification within a few hundred thousand years or so (or at 10% total shortening or less), and that the model thermal profiles would have reached nearly steady state at the end of each run. Some simulations failed to run to the specified durations because either the stress change or strain change tolerance was violated in one or more near-surface elements, leading to convergence failure at one or more nodes. We discuss the reasons for this below in section 4.1.

**Table 2.** Summary of Model Results[a]

| Run | Creep Law[b] | $T_s$, K | $T_o$, K | $\dot{\varepsilon}_{app}$, $s^{-1}$ | c, MPa | κ, $m^2/s$ | ρ, $kg/m^3$ | Final Short, % | Total Time, $\times 10^6$ yr | Max Relief, m | Short at 10 m, % | Time at 10 m, $\times 10^6$ yr |
|---|---|---|---|---|---|---|---|---|---|---|---|---|
| *Runs That Achieved at Least 10 m Topographic Relief* | | | | | | | | | | | | |
| A | M | 1000 | 1300 | 5.0e-14 | 50 | 1.0e-6 | 2900 | 55.4 | 0.52 | 15.6 | 55.4 | 0.52 |
| B | M | 1000 | 1300 | 1.0e-14 | 50 | 1.0e-6 | 2900 | 71.7 | 4.00 | 38.4 | 61.3 | 3.01 |
| C | M | 1000 | 1200 | 1.0e-14 | 50 | 1.0e-6 | 2900 | 73.1 | 4.16 | 39.0 | 61.1 | 2.99 |
| D | M | 1000 | 1300 | 3.0e-14 | 50 | 1.0e-6 | 2900 | 64.9 | 1.11 | 54.4 | 48.6 | 0.70 |
| E | M | 1000 | 1300 | 4.0e-14 | 50 | 1.0e-6 | 2900 | 53.7 | 0.61 | 13.3 | 47.0 | 0.50 |
| F | C | 975 | 1300 | 7.0e-15 | 30 | 8.0e-7 | 2900 | 64.4 | 4.68 | 34.8 | 58.6 | 4.00 |
| G | C | 975 | 1300 | 7.0e-15 | 30 | 8.0e-7 | 2900 | 42.4 | 2.50 | 10.1 | 42.4 | 2.50 |
| H | C | 975 | 1300 | 4.0e-15 | 30 | 8.0e-7 | 2900 | 71.7 | 10.0 | 31.8 | 53.1 | 6.01 |
| I | C | 950 | 1300 | 4.0e-15 | 30 | 8.0e-7 | 2900 | 66.7 | 8.74 | 63.0 | 46.8 | 5.00 |
| J | C | 960 | 1300 | 4.0e-15 | 30 | 8.0e-7 | 2900 | 65.1 | 8.35 | 47.4 | 46.8 | 4.99 |
| K | M | 1000 | 1300 | 2.0e-15 | 30 | 8.0e-7 | 2900 | 46.8 | 10.0 | 13.2 | 46.8 | 10.0 |
| *Runs That Did Not Achieve 10 m Topographic Relief* | | | | | | | | | | | | |
| l | M | 975 | 1400 | 5.0e-14 | 50 | 1.0e-6 | 2900 | 52.2 | 0.47 | 5.8 | – | – |
| m | M | 1000 | 1500 | 1.0e-13 | 50 | 1.0e-6 | 2900 | 56.7 | 0.53 | 6.1 | – | – |
| n | M | 987 | 1300 | 5.0e-14 | 50 | 1.0e-6 | 2900 | 47.1 | 0.40 | 4.7 | – | – |
| o | M | 987 | 1300 | 4.0e-14 | 50 | 1.0e-6 | 2900 | 48.0 | 0.52 | 5.5 | – | – |
| p | M | 1000 | 1300 | 3.0e-14 | 50 | 1.0e-6 | 2700 | 30.0 | 0.38 | 2.6 | – | – |
| q | C | 975 | 1300 | 5.0e-14 | 50 | 1.0e-6 | 2700 | 33.0 | 0.26 | 4.5 | – | – |
| r | C | 950 | 1300 | 5.0e-14 | 50 | 1.0e-6 | 2700 | 28.8 | 0.36 | 4.3 | – | – |
| s | C | 950 | 1300 | 3.0e-14 | 30 | 8.0e-7 | 2900 | 21.7 | 0.26 | 1.6 | – | – |
| t | C | 950 | 1300 | 3.0e-14 | 30 | 1.0e-6 | 2900 | 42.3 | 0.50 | 6.4 | – | – |
| u | C | 950 | 1300 | 5.0e-14 | 30 | 8.0e-7 | 2900 | 46.8 | 0.40 | 6.2 | – | – |
| v | C | 975 | 1300 | 7.0e-14 | 30 | 8.0e-7 | 2900 | 12.1 | 0.06 | 0.7 | – | – |
| w | C | 960 | 1300 | 5.0e-14 | 30 | 8.0e-7 | 2900 | 41.7 | 0.34 | 4.7 | – | – |
| x | C | 1000 | 1300 | 5.0e-14 | 30 | 8.0e-7 | 2900 | 19.1 | 0.13 | 1.8 | – | – |
| y | C | 975 | 1300 | 5.0e-14 | 30 | 8.0e-7 | 2900 | 10.5 | 0.07 | 0.8 | – | – |
| z | C | 975 | 1300 | 1.0e-14 | 30 | 8.0e-7 | 2900 | 33.9 | 1.32 | 4.4 | – | – |
| aa | C | 960 | 1300 | 1.0e-14 | 25 | 8.0e-7 | 2900 | 9.4 | 0.31 | 0.8 | – | – |
| bb | C | 960 | 1300 | 1.0e-14 | 30 | 8.0e-7 | 2900 | 25.2 | 0.92 | 2.9 | – | – |
| cc | M | 975 | 1300 | 4.0e-15 | 30 | 8.0e-7 | 2900 | 37.3 | 3.70 | 5.3 | – | – |
| dd | M | 1000 | 1300 | 4.0e-15 | 30 | 8.0e-7 | 2900 | 37.9 | 3.78 | 5.7 | – | – |
| ee | M | 975 | 1300 | 2.0e-15 | 30 | 8.0e-7 | 2900 | 23.7 | 4.29 | 2.6 | – | – |

[a] $T_s$, surface temperature; $T_o$, initial interior temperature; $\dot{\varepsilon}_{app}$, applied shortening rate; c, cohesion; κ, thermal diffusivity; ρ, density.
[b] C, Columbia diabase; M, Maryland diabase.

The run times achieved by each simulation these correspond to 3000–23000 time increments and are noted in Table 2.

[19] A typical finite element mesh is shown schematically in Figure 2. We used three different meshes, containing between 9232 and 32000 four-node quadrilateral plane-strain elements. High mesh resolution near the surface was required both horizontally (to ensure adequate sampling of the topography at short wavelengths and to prevent aliasing of high spatial-frequency components into other parts of the spectrum) and vertically (to allow monitoring of changes in the mechanical properties at the mesh cooled from the surface downward). All of the meshes were constructed with increasing mesh resolution toward the top. Meshes A–E and l–o (Table 2) were 3 km wide by 3 km deep and had initial element dimensions at the surface of 5.86 m wide by 5.86 m high; runs F and p–bb (6 × 3 km) had surface elements 5.86 × 3.75 m; and runs G–K and cc–ee (6 km × 3 km) had surface elements 11.7 × 10 m.

[20] The mesh topography was sampled at intervals corresponding to the horizontal spacing of the nodes across the top of a mesh. For evenly spaced data points, calculation of the Fourier spectral content of each mesh's topography would involve a straightforward spatial Fourier transform; however, though the mesh nodes were equally spaced initially, they became unevenly distributed as deformation proceeded. Furthermore, successively higher frequency components were introduced as the meshes became finer with progressive shortening. To account for these factors, we calculated the amplitude spectra using the Lomb-Scargle Fourier transform method for unevenly spaced series presented by *Scargle* [1982, 1989], and implemented by *Schulz and Stattegger* [1997]. The wavelengths of interest were between 100 m and 1 km; because the initial horizontal node spacing ranged from 5.86 to 11.7 m, the topographic profiles were well oversampled. We did not consider wavelength components longer than 1 km.

[21] To initiate a compressional instability, the surface of each model was perturbed with small-amplitude random topographic perturbations at each node (Figure 3). The three perturbations used were intended to represent random infinitesimal flaws in the surface of the deforming rock; without these perturbations, the meshes would simply have shortened homogeneously. We tested three different perturbations to ensure that the results were independent of the perturbation shape, and we varied the degree of smoothness to eliminate any spurious geometric effects due to jagged initial topography. The left vertical boundary of each mesh was held fixed horizontally, and a horizontal velocity $u(t)$ was applied to the right edge to give a constant proportional displacement rate;

$$\dot{\varepsilon}_{app} = \frac{d}{dt}\left(\frac{\delta x}{x}\right) = \text{constant}, \tag{7}$$

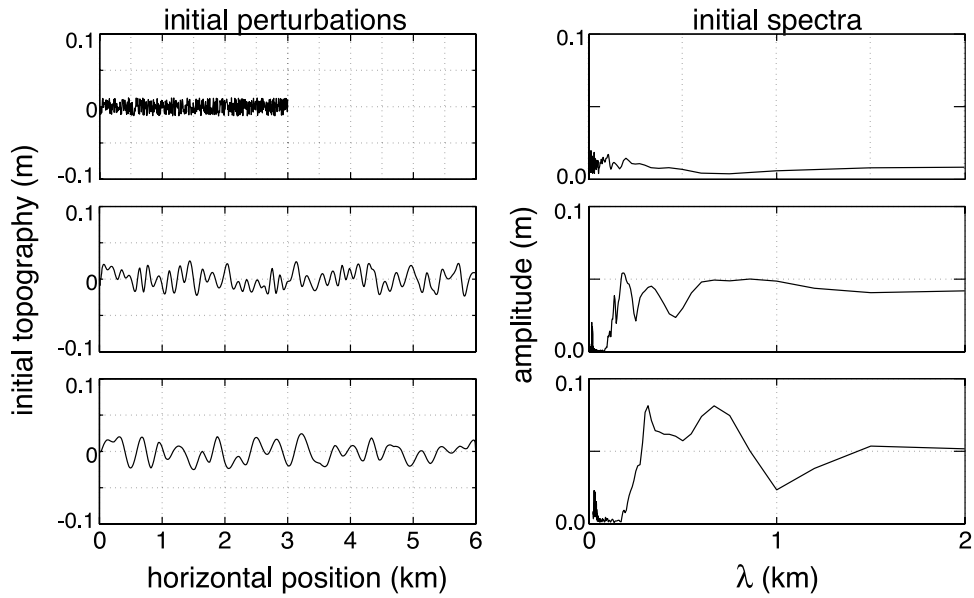


**Figure 3.** Three (left) initial infinitesimal topographic perturbations and (right) spatial frequency domain amplitude spectra used in our finite element models. The amplitude spectra are truncated at 2 km to show the short-wavelength detail.

where $\delta x$ is the incremental displacement of the right edge and $x$ is its current $x$ coordinate. An elastic Winkler foundation was applied at the base of each mesh, so that in the initial time step, the mesh fell vertically to a level at which its weight was compensated by the restoring force of the elastic foundation. This allowed the base of the mesh to deform vertically as well as horizontally, and eliminated effects from the base on vertical displacements elsewhere in the mesh; in addition, as discussed in section 4.3, rapid creep in the deep parts of each mesh effectively decoupled the base from the near-surface region. The initial rigid body translation due to gravity was removed in subsequent calculations. To counteract Poisson stresses induced by gravitational body forces and the applied normal force representing the weight of the atmosphere (92 bars), we used a lithostatic reference stress state ($\Delta\sigma = 0$ [e.g., *Albert and Phillips*, 2000; *Nunes et al.*, 2004]).

[22] For the thermal evolution, we used a 1-D transient half-space cooling model [*Turcotte and Schubert*, 1982, p. 158] with a uniform initial interior temperature $T_0$ and an instantaneous shift in surface temperature at time 0 to a value $T_s$ ($<T_0$; constant for $t > 0$). The thermal behavior is given by

$$T = T_0 + (T_s - T_0)erfc\frac{y}{2\sqrt{\kappa t}}, \tag{8}$$

where $y$ is the depth below a reference surface and $\kappa$ is thermal conductivity. A typical cooling profile is shown in Figure 4. This expression does not include an advective term corresponding to motion of the material in the mesh; this does not introduce significant errors because the rate of horizontal motion of mesh nodes is significantly slower than the rate of conductive cooling in the shallow crust, and the scale of horizontal and vertical motions of mesh material are so small relative to the extent of the thermal influence of the plume that advective effects would represent very small adjustments to the background vertical conduction (Figure 2). We coupled the thermal and mechanical solutions by calculating the temperature at each node in the mesh at each time step using that node's position relative to a reference surface, and then using that calculated temperature to calculate the corresponding creep strain increment. The new position of each node was then calculated, and used to recalculate the temperature at the next time step. Values for $T_0$ and $T_s$ for each run are given in Table 2. For simplicity, all material properties (save creep) were independent of temperature, and thermal expansion was not included. Recent work has shown that thermal conductivity can depend in a significant way on temperature [*Hofmeister*, 1999]. Depending on the sign of the temperature dependence over the relevant temperature

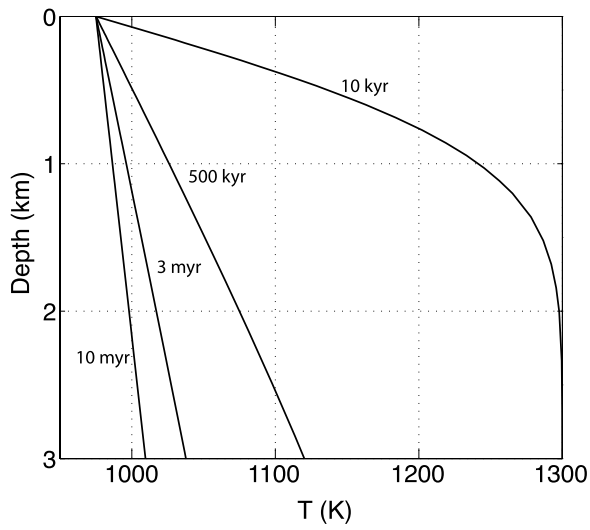


**Figure 4.** Plot showing model temperature versus depth at four time steps for run H.

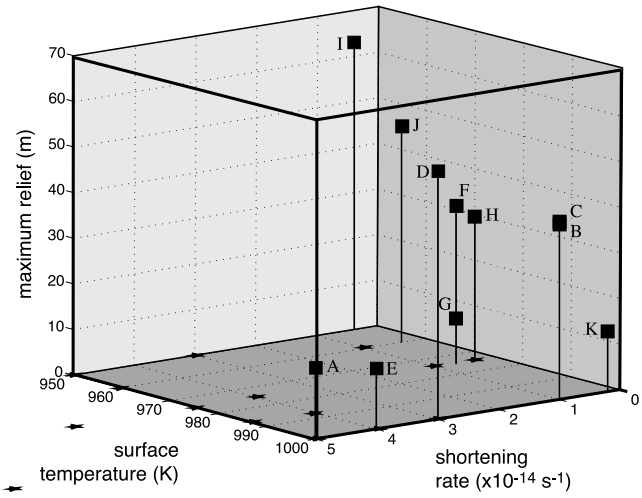


**Figure 5.** Model topographic relief as a function of input parameters surface temperature and applied shortening rate. Models that failed to achieve 10 m of relief (stars) are also shown.

range, this could act either to slow the model cooling and promote creep, or to accelerate cooling and create a positive feedback between decreasing temperature and thermal conductivity. To accommodate this to first order, we used two different values for thermal diffusivity (Table 2), but we did not explore the effects of this parameter exhaustively. For simulating cooling above a plume, $T_0$ could have a wide range of values, depending on the strength of the plume, the degree to which it penetrates the lithosphere, or the length of time the plume generates a thermal influence at shallow levels, to name but three factors. The only real constraint is that it should be lower than the solidus temperature of anhydrous Maryland or Columbia diabase at the appropriate depth.

[23] Surface temperatures as high as those used in this work might eventually lead to viscous relaxation of plateau topography. *Nunes et al.* [2004] addressed the relaxation characteristics of isostatically compensated plateaus under surface temperatures of 740 K and 940 K, and found that significant topographic relaxation can occur at long wavelengths on timescales of $10^8$ years for hot conditions (940 K surface temperature and high basal heat flux). Uncompensated plateau topography would likely relax more quickly under hot conditions; however, the structures simulated in the current work are a few meters high, with wavelengths less than 1 km, and would likely be compensated by the strength of the crust, even if that strength is rather low, as outlined in the following sections. Thus, even if long-wavelength topographic relaxation were occurring concurrently with and on similar timescales as formation of the short-wavelength tectonic structures, the scale and morphology of the structures so formed would not be greatly affected. Furthermore, the observed persistence of plateau topography to the present time argues against prohibitive degrees of topographic relaxation in the early stages of plateau formation.

[24] The simulations used an updated Lagrangian procedure, in which the finite element mesh is fixed to the material, but the reference frame for each time step is the last completed increment rather than the initial configuration. This scheme is appropriate for situations in which permanent deformations are large. MARC has parallel capabilities, allowing use of multiple processors either on a single machine or multiple machines connected on a network. The models presented here were calculated using twelve processors on the SGI Origin 2000 supercomputer in the Center for Scientific Parallel Computing at Washington University in St. Louis (http://harpo.wustl.edu). The meshes were decomposed vertically into 12 domains, and each domain was sent to a different processor for evaluation. The domains were constructed to minimize the number of interdomain nodes and to allot approximately equal numbers of elements to each domain, minimizing computation time devoted to interdomain communication. Using 12 domains, the model runs typically used 12–24 hours of computation time.

## 4. Results

### 4.1. Requirements for Formation of Short-Wavelength Ridges

[25] The results for all 31 simulations are summarized in Table 2. Eleven of these developed short-wavelength topography with crest-to-crest spacing $\leq$1 km and total relief $\geq$10 m, and were thus deemed successful. Figure 5 shows the total relief achieved by each of these runs as functions of $T_s$ and $\dot{\varepsilon}_{app}$. Formation of the target structures on the desired scales was possible only for a restricted range of parameters. Some simulations with too high a shortening rate and/or too low a temperature were able to build up large stresses in regions of high slope near the surface. Because new load increments were imposed at each time step, these stresses sometimes increased faster than they could be relaxed by creep, causing the yield stress to be exceeded, and large plastic strains occurred. In these cases, if the plastic strain change relative to the elastic strain was sufficiently large, this caused a violation of the strain change tolerance (or the stress change tolerance if the corresponding stress drop was too large), even for a very small time step; this sequence led to termination of the run. For some runs, this occurred at long geological times, when very large degrees of total shortening, and thus large element distortions, had occurred. The termination of these runs was not considered premature. For other runs, this convergence failure occurred much earlier. For example, run v ended at a simulated geological time of $\sim$60 kyr, after experiencing 12% total shortening and only 0.7 m of topographic relief. By contrast, run F, which used the same mesh as run v, ran to 4.68 Myr and experienced 64.4% total shortening and 34.8 m of relief. The only difference between these two runs was that run v used a faster applied shortening rate than did run F. As outlined in section 3, we used three different model resolutions in part to ensure that the convergence issues were not simply related to mesh resolution. Increasing the mesh resolution did not result in better convergence characteristics. It is possible that using a different plasticity criterion could change this behavior; however, on the basis of the results derived from runs that did not experience early convergence failure, we determined that additional investigation of this issue is beyond the scope of the usefulness of the current results. We discuss this in more detail in section 5.2.

[26] Other simulations with relatively high integrated strength developed topography on scales longer than the desired 1 km; in many cases, these models developed only a partial wavelength across the entire mesh. At the opposite extreme, excessively high temperatures and/or low shortening rates caused creep strains to relax the model stresses so efficiently that topographic amplification occurred too slowly to produce appreciable relief, even at high degrees of total shortening. Successful runs were achieved for $T_s$ of 950 K to 975 K and shortening rates of $7 \times 10^{-15}$ s$^{-1}$ to $4 \times 10^{-15}$ s$^{-1}$ using the Columbia diabase creep law; models using the stronger Maryland diabase were successful only for $T_s$ = 1000 K (the highest value considered) but a larger range of shortening rates, from $2 \times 10^{-15}$ s$^{-1}$ to $5 \times 10^{-14}$ s$^{-1}$. Variations in $T_0$ had negligible effects on the results (Table 2, Figures 4 and 5) because the timescale of conductive cooling near the surface was much faster than the timescale for topographic amplification.

### 4.2. Topography

[27] Topographic profiles at three time steps during each successful run are shown in Figure 6a. The topography for all the runs are shown at the same scale, but the plots for the three time steps are offset along a common axis for clarity. It is apparent from these plots that most of the macroscopic amplification of topography occurred during the end stages of each run, at high values of total shortening. In fact, all of the successful runs experienced at least 40% bulk shortening before the desired 10 m of relief were achieved. Fourier amplitude spectra for these profiles are shown in Figure 6b. It should be noted that these plots show Fourier amplitude versus spatial wavelength, which is not the same as the topographic relief. The total relief used to determine "success" was simply the difference between the highest and lowest points in the final topography; this is a less restrictive criterion than a 10 m threshold on the Fourier amplitude. All of the spectra show a major peak near 1 km, corresponding to a long-wavelength warp across the top of the mesh. In addition, all show peaks at wavelengths less than 1 km with amplitudes at least 1/4 that of the largest peak. The presence of multiple wavelengths in the topographic spectra is in agreement with the observation of multiple ridge wavelengths in Venusian crustal plateau marginal ridge belts. All of the runs were initially strongly influenced by the initial perturbations, but eventually developed their own distinct spectral characteristics.

### 4.3. Strain Partitioning

[28] The presence of multiple wavelengths of deformation in our simulations indicates mechanical heterogeneity within the deforming parts of the mesh. This heterogeneity arises in response to local P-T-$\dot{\varepsilon}$ conditions, and is unique to each simulation. To illustrate the key behaviors we observe in successful runs, we show detailed results for simulations H and I in Figures 7 and 8.

[29] Figures 7a and 7b show plots of differential stress versus depth along two vertical profiles through simulation I, calculated at the final time increment; the locations of these profiles are shown in the contour plot of differential stress in Figure 7c. The differential stress distribution in the mesh at any time represents the strength of the material at each point, and results from the combined effects of the imposed loading and the material's response. Both the stress profiles and the contour plot show that the differential stress distribution in the mesh is heterogeneous above ~1 km depth. In this shallow region, the mesh exhibits regions that are relatively strong (i.e., are able to support relatively high stresses) and others that are relatively weak. Below ~1 km, the differential stress decreases smoothly as a power law function of depth.

[30] It is apparent from these plots that simulation I does not develop a sharp mechanical discontinuity between two mono-rheological layers, but instead develops a near-surface region of mixed mechanical properties. Plastic and creep strain rates versus depth for the same two profiles are shown in Figures 7d and 7e, and the corresponding contour plot of plastic strain rate is shown in Figure 7f. Below ~1 km, the plastic strain rate drops rapidly to zero, and all of the deformation in the lower region of the mesh is accommodated by creep, as expected. The exact depth of this transition varies laterally, mirroring the long-wavelength surface deformation. Above this transition, both plastic and creep strain rates vary significantly across the mesh. At some locations, the plastic strain rate exceeds the creep strain rate, whereas the two are comparable in other regions. The contour plot of plastic strain rate (Figure 7f) shows that plastic strain rates, and therefore plastic strains, are highest beneath topographic highs, indicating that the largest degree of brittle deformation occurs in those locations. These high plastic strain rate regions correspond spatially with regions of intermediate to low differential stress, indicating that stresses in these locations in the mesh are relieved significantly by plastic failure.

[31] On the other hand, creep strains are favored by high stresses (equations (5) and (6)), so that even in these shallow regions, creep strains are significant in regions where plastic strains do not efficiently relieve stresses (Figures 7d and 7e). Along profile A, for example, though the plastic strain rate exceeds the creep strain rate above ~400 m, the creep strain rate remains high and is roughly one-half the plastic strain rate at the surface. Along profile B, the creep strain rate is even higher relative to the plastic strain rate at all depths, and the two are equal at the surface. Because of the high temperatures used in these simulations, creep constitutes the steady state background deformation mechanism everywhere in the mesh, even at the surface. Plastic strains are superimposed on this background mode in the near-surface heterogeneous zone. Though our simulations cannot distinguish between localized faulting or frictional slip and distributed cracking on micro- or macroscopic scales, the deformation in this region resembles the semibrittle deformation described by *Kohlstedt et al.* [1995], which those authors define as the simultaneous action of small-scale distributed faulting and crystal-scale creep. This interpretation is reasonable, given the stress and temperature conditions in the meshes, and we use this definition hereafter in discussing the near-surface regions of our finite element models. Rather than a sharp discontinuity between two mono-rheological layers (i.e., brittle above and ductile below), the near-surface region of mesh I shows a deformation style characteristic of a diffuse brittle-ductile or brittle-plastic transition zone. Similar behavior was observed by *Albert and Phillips*

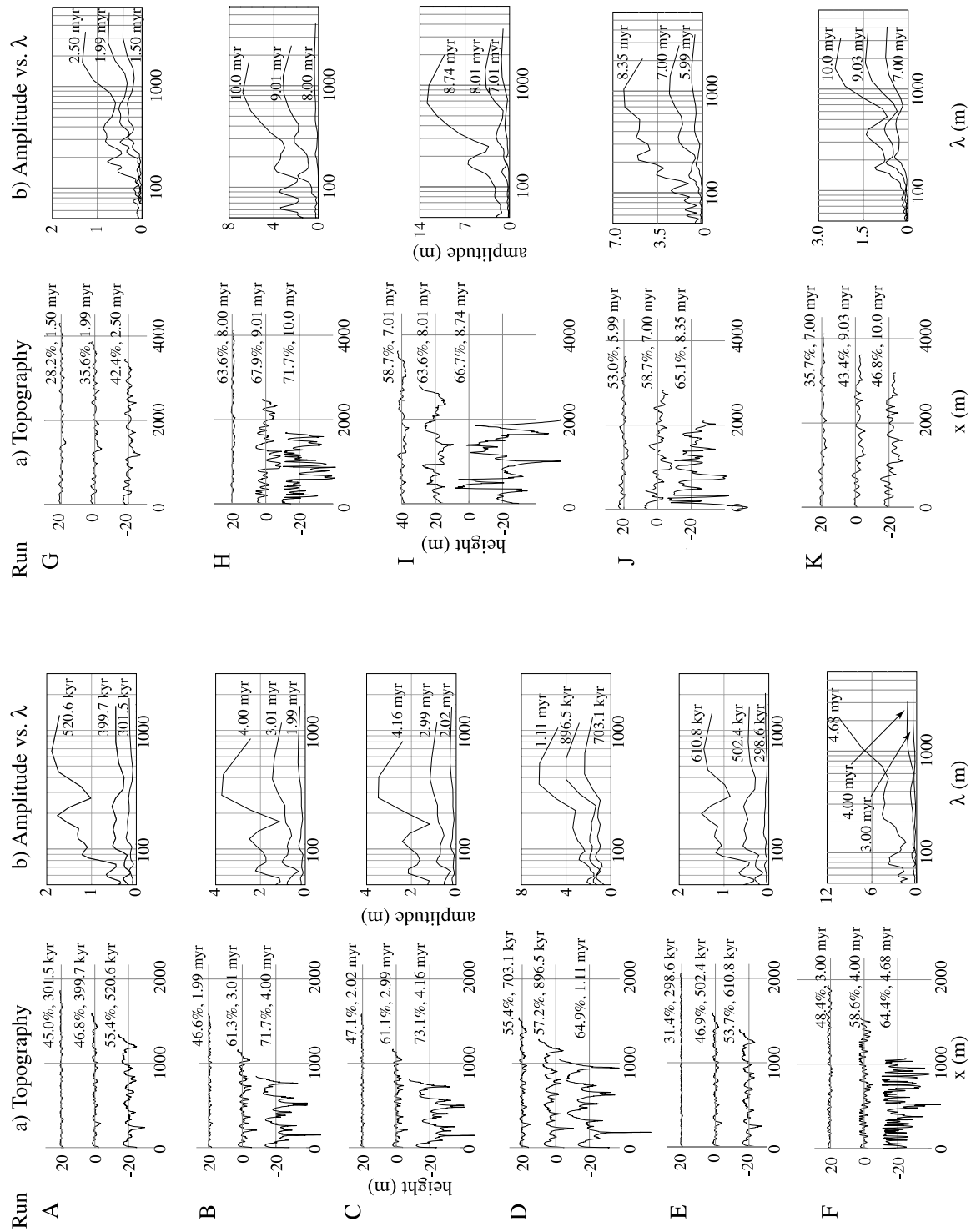


**Figure 6.** Plots showing (a) topographic profiles and (b) Fourier amplitude versus wavelength λ (shown on a log scale) at three time steps. Profiles for the three time steps in Figure 6a are offset along a common axis for clarity, and time steps are labeled with total shortening (as a percentage) as well as total time elapsed. Spectra in Figure 6b are shown on the same axes, with no offsets.

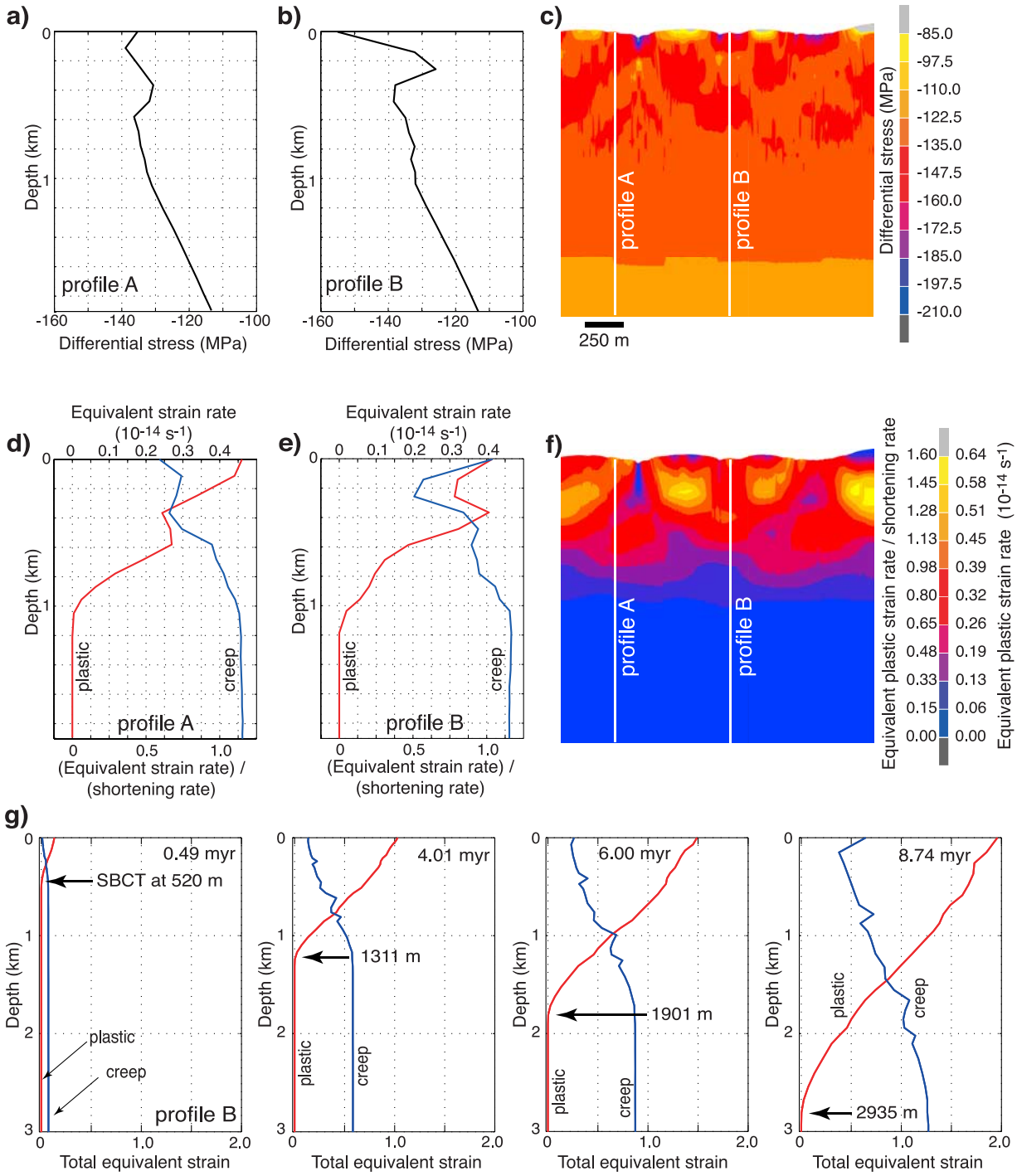


**Figure 7.** Results for simulation I. (a and b) Plots of differential stress (tension positive) versus depth for two profiles at the final time step; (c) contour plot of differential stress at the final time step; (d and e) plots of creep and plastic strain rate versus depth for two profiles at the final time step; (f) contour plot of plastic strain rate at the final time step; and (g) plots of total creep and plastic strains versus depth at four time steps. All strains and strain rates are equivalent quantities and so include all of the tensor components. Strain rate plots show absolute equivalent strain rates as well as strain rates as fractions of the applied shortening rate. The contour plots are shown with no vertical exaggeration but are truncated below the upper heterogeneous zone.

[2002] in narrow zones beneath the topographic loads in their models of flexure of the oceanic lithosphere, and was similarly interpreted to represent distributed microfaulting plus creep. Because of the prominence of creep at all depths, no purely brittle layer develops in this simulation, so the top of this distributed brittle-plastic transition zone predicted by rock deformation experiments (e.g., those summarized by *Kohlstedt et al.* [1995]) and observed in

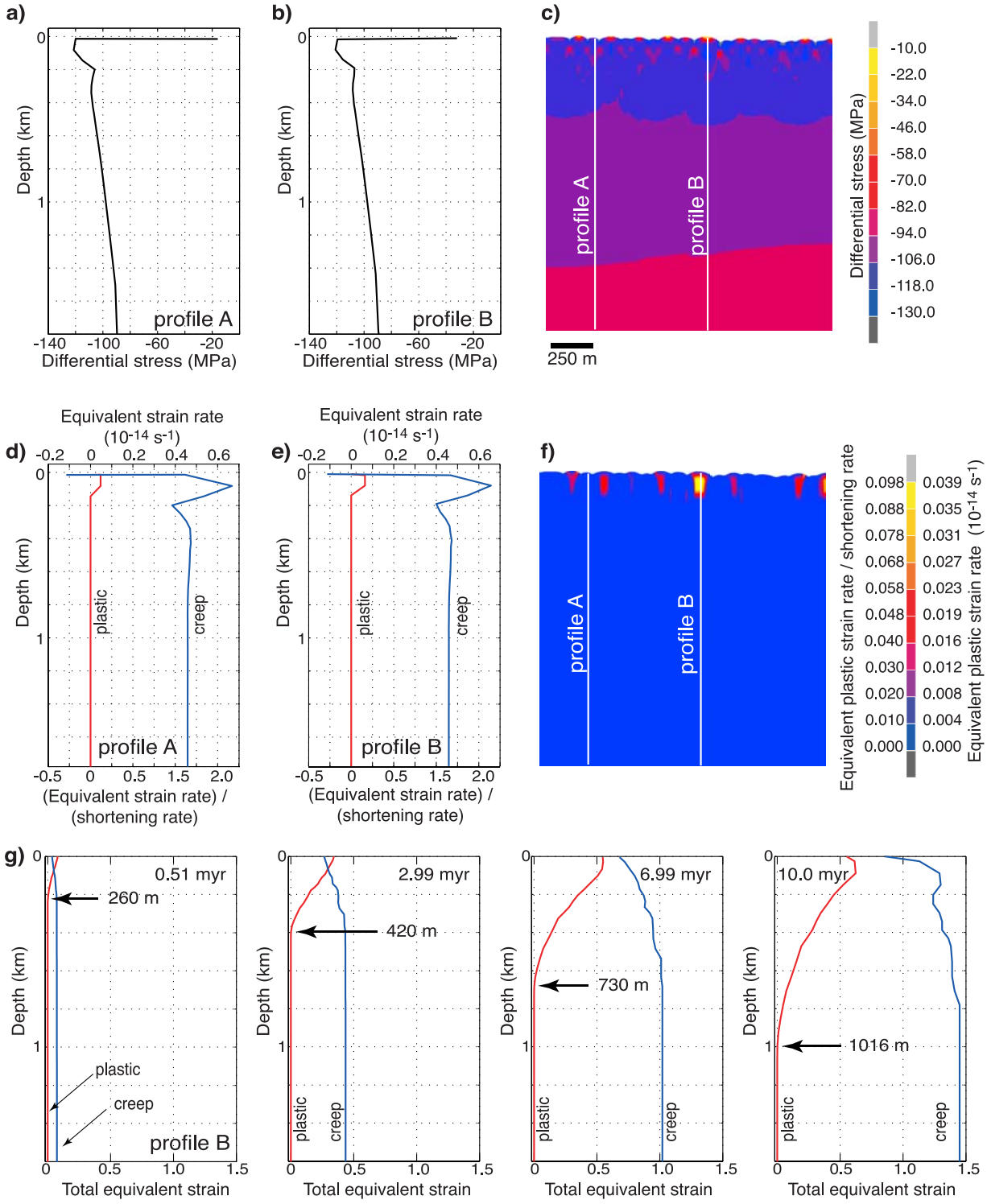


**Figure 8.** Results for simulation H, following Figure 7.

the finite element models of *Albert and Phillips* [2002] is not realized.

[32] Plots of the total accumulated plastic and creep strains along profile B at four time steps are shown in Figure 7g, representing snapshots at each time step of the aggregate rheology developed in mesh I over its modeled history in response to continued loading and cooling. At any time, the base of the semibrittle zone is defined by the depth at which the total plastic strain goes to zero; we term this the "semibrittle to creep transition", or SBCT. The depth to the SBCT increases with time in run I from ~0.5 km at 0.5 Myr to nearly 3 km at 8.74 Myr. Plasticity becomes more important at deeper levels with time because the models are continually cooling downward from the surface; thus the semibrittle to creep transition migrates downward with time. Creep strains also increase continually throughout the run,

even at the surface, because the mesh is subjected to continuous loading.

[33] Simulation H represents the other extreme of the range of behavior exhibited in the successful simulations. Plots of differential stress along profiles A and B, and a contour map of the stress distribution, are shown in Figures 8a–8c. These plots, like those for run I, show heterogeneities in the stress distribution in the upper part of the mesh; however, the total variation in stress is less than that for run I, and the differences between profiles A and B are small. Examination of the plots of creep and plastic strain rates (Figures 8d–8f) show that like run I, the upper several hundred meters of mesh H is semibrittle, and the highest plastic strain rates occur beneath topographic highs. However, the plastic strain rate is at most roughly an order of magnitude smaller than the creep strain rate. The total inelastic strains at four time steps (Figure 8g) show that like simulation I, the depth to the SBCT increases with time; however, creep strains increase faster than plastic strains at all depths, so that between 3 and 7 Myr in the run, creep strains begin to exceed plastic strains everywhere. At the final time step, the total equivalent plastic strain is nonzero above 1016 m, but contributes only a fraction of the total inelastic strain, even at the surface.

[34] The marked differences between simulations H and I are due entirely to a 25 K difference in surface temperature; all other parameters (including mesh resolution and initial perturbation) are identical (Table 2). The other successful model runs fall into the range of behavior spanned by these two examples. The details of the variation in behavior from one run to another are functions of the variable parameters, with $T_s$ the most important variable, followed by $\dot{\varepsilon}_{app}$. We tested a number of combinations of these parameters in order to explore the parameter space thoroughly (Figure 5, Table 2). In the next section, we outline the general observations that resulted from this exploration.

### 4.4. Summary of Results

[35] The eleven successful model runs indicate that (1) using the conditions proposed by *Phillips and Hansen* [1998], it is possible to achieve contractional tectonic structures with a range of wavelengths less than 1 km, but only within a restricted range of parameters; (2) none of the simulations developed a near-surface brittle layer or a BDT, but rather developed a near-surface semibrittle zone defined by the simultaneous action of plasticity and creep; and (3) total mesh shortening in excess of 40% was required to achieve a modest 10 m of total topographic relief.

## 5. Discussion

[36] An important idea proposed by *Hansen and Willis* [1998] that in part led to the refinement of the plume hypothesis by *Phillips and Hansen* [1998] is that as crustal plateau lithosphere cooled from its initially hot, weak state, a brittle surface layer would develop, separated from the underlying material by a sharp décollement, and the thickness of this layer at any time would control the wavelength of the structures formed at the same time. The presence of multiple structural suites with unique characteristic wavelengths was interpreted to indicate a progressive thickening of the layer with continued cooling [e.g., *Hansen and Willis*, 1998; *Ghent and Hansen*, 1999; *Hansen et al.*, 2000]. To the extent to which the rheological model used here accurately represents the real Venusian lithosphere, we can evaluate those ideas in light of our results.

### 5.1. Importance of Plasticity to Structural Deformation

[37] Because of the high temperatures used in these runs, the simulations did not develop near-surface brittle layers. Instead, each mesh developed a semibrittle near-surface region in which brittle and creep mechanisms operated simultaneously. The thickness of this layer was most strongly influenced by the surface temperature and secondarily by the shortening rate. Comparison of Figures 7 and 8 with the Fourier spectra for the appropriate meshes in Figure 6b shows that a qualitative relationship exists between the depth to the SBCT and the wavelength of topography that develops at the mesh surface. For example, the topography for run I, with an SBCT at ~3 km at the final time step, has a longer characteristic wavelength than that for run H, with an SBCT at only ~1 km at the final time step. The spectra for runs H and I (Figure 6b) both show significant peaks near 1 km, but the amplitude of this peak is much greater for run I than for run H; furthermore, the spectrum for run H shows three shorter-wavelength peaks with amplitudes greater than half that of the dominant peak, whereas spectrum I shows only one short-wavelength peak. This relationship between structural wavelength and thickness of the semibrittle zone is an interesting result, because it indicates that the action of plasticity in the upper parts of the meshes, however small relative to the background creep strain, affects the mechanical behavior of the model material in a significant way.

[38] This relationship tempts us to compare the wavelength-to-layer thickness ratios we observe in the finite element runs with the predictions of classical theoretical and numerical fold models [e.g., *Biot*, 1961; *Ramberg*, 1962; *Fletcher*, 1974; *Smith*, 1977, 1979; *Zuber and Parmentier*, 1996] or with the finite element results such as those of *Mancktelow* [1999] or *Zhang et al.* [1996, 2000]. Such a comparison is problematic, however, first because those studies commonly use a model with power law viscous or viscoelastic layers of fixed thickness embedded in a matrix of similar rheology. Our material is not viscous or viscoelastic, but rather elastoviscoplastic, and (as we have seen) the addition of plasticity provides an additional mechanism for relief of loading stresses relative to the viscoelastic models, fundamentally changing the mechanical characteristics of the problem. Other treatments of this problem, such as the theoretical work of *Montési and Zuber* [2002, 2003], employ a strongly localizing layer (formulated to include plasticity, if appropriate) over a nonlocalizing substrate. However, as outlined in section 3, growth of structures in these single-layer folding models requires a boundary between the two layers across which the mechanical properties are discontinuous; our MARC meshes do not develop distinct mechanical layers separated by a sharp décollement, and do not experience strong competence contrasts across boundaries. Furthermore, the continuous cooling experienced by our meshes causes the thickness of the upper semibrittle layer to change with time, and it is not immediately clear how the timescale over which this

layer thickens relates to the timescales on which incipient contractional features develop their preferred wavelengths. Finally, the wavelength characteristics and growth rates calculated in the analytical models hold only at very small values of total strain, whereas growth of contractional structures does not become appreciable in our simulations except at large total strains.

[39] The evolution of our simulations' near-surface semibrittle zone is consistent with the predictions of a cooling lithosphere model, in that the SBCT deepens with cooling. The spectra shown in Figure 6b indicate that the longest-wavelength topographic components amplify significantly with cooling, which is also broadly consistent with the plume hypothesis. However, the time evolution of the SBCT (Figures 7g and 8g) and the development of the corresponding topographic spectra (Figure 6b) for runs H and I highlight the complex relationship between changes in layer thickness and structural wavelengths. If there were a direct one-to-one relationship between the depth to the SBCT and structural wavelengths at any time, we would predict that progressively longer structural wavelengths would become dominant in response to the thickening semibrittle surface layer. This is not the case, however. For instance, the topographic spectra for runs H and I show that several new short-wavelength components appear in the last two time steps, even though the SBCT is concurrently becoming deeper in both runs. Furthermore, none of the runs develops appreciable structural relief until the last few time steps, when a large degree of total shortening has occurred. For both runs H and I, virtually all of the structural relief achieved occurs between the last two increments depicted in Figures 7g and 8g. The depth to the SBCT at those times would correspond to folding wavelengths on the order of 4–12 km according to the commonly used wavelength-to-layer thickness ratio of 2–4. Contrary to these predictions, the largest spectral peaks for these runs at all time steps are at wavelengths <1 km, and shorter-wavelength peaks account for a larger proportion of the total spectral content at later time steps than at earlier ones. Thus the expected progression from short-wavelength to long-wavelength dominated spectra is not observed, and so the wavelength progression of tectonic features with time is inconsistent with the predictions of the plume hypothesis.

[40] Though our meshes do not develop a brittle surface layer whose thickness directly controls the structural wavelengths, the presence of plasticity in the upper heterogeneous layer in our meshes clearly affects the bulk mechanical character of the layer. Aside from the implications this has for formation of crustal plateau folds, these results may also shed light on the general behavior of rocks in the semibrittle regime (as used here) under compression. Analysis of simulations similar to those presented here using different material properties and thermal characteristics may provide a new avenue for understanding the physics of cataclastic and semibrittle deformation in the cores of folds or along fault surfaces.

### 5.2. Implications for Formation of Crustal Plateau Structures

[41] We have seen that the thickness of the semibrittle layer influences the topographic wavelengths developed in the finite element meshes, and that the most significant factor controlling the layer thickness is the surface temperature, $T_s$. However, the absence of a near-surface brittle layer, and the complicated relationship between the downward migration of the SBCT and the resulting structural wavelengths, indicate that the relationship between the rheology of the cooling layer and the contractional features is more complicated than previously envisioned. In addition, the high degree of total shortening required to achieve 10 m of topographic relief in the meshes is cause for concern. Topographic amplification in all the simulations was negligible until a bulk shortening of ~25% was reached, and none of the models developed the desired 10 m of total relief with total shortening less than 40%. This is a direct consequence of the low effective strength of even the ultra-dry diabase used in the models under the unusually hot conditions proposed. The source of such inordinately large horizontal strains in the context of the plume hypothesis is unclear; such high degrees of shortening seem geologically implausible. One possible mechanism is coupling of shear stresses into the base of thin Venusian lithosphere over a dynamically supported swell during the active period of plume-lithosphere interaction, as suggested by *Phillips* [1986, 1990], which might cause significant stretching forces in the lithosphere, and high degrees of contraction at the uplift margins. Simulations using shear tractions at the base of the crust could be conducted to determine whether or not this type of process could produce the necessary shortening.

[42] The positions of the model runs that yielded at least 10 m of vertical relief are shown on a plot of total shortening versus surface temperature in Figure 9. This plot illustrates the difficulty with which the desired results were achieved. On one hand, high $T_s$ is required to produce structures with wavelengths $\leq$1 km. On the other hand, rather than creating conditions under which short-wavelength contractional structures develop readily in response to shortening, the drastically elevated surface temperature instead inhibits the development of these structures by weakening the material so that it cannot support significant topographic amplification until an unrealistic degree of horizontal strain has occurred. This leads us to reconsider whether such a high surface temperature is actually required to achieve short-wavelength, spatially periodic tectonic deformation in the context of a plume impinging on thin lithosphere. Another potentially deleterious consequence of the high surface temperature is the predominance of creep at shallow depths in the meshes, which leads to the semibrittle rheology that we observe near the mesh surfaces, analogous to the small-scale, distributed brittle faulting that together with microscopic creep defines the semibrittle rheology discussed by *Kohlstedt et al.* [1995]. This seems inconsistent with the purely brittle, spatially localized faulting that characterizes ribbon structures [*Hansen and Willis*, 1996, 1998, and references therein; *Ghent and Hansen*, 1999].

[43] On the basis of the above points, it seems that either (1) if our models accurately represent the most salient features of the rheology of the actual rocks, then a drastically (and long-lasting) elevated surface temperature actually inhibits the formation of the desired structures, and so the requirement for such a high temperature should be relaxed,

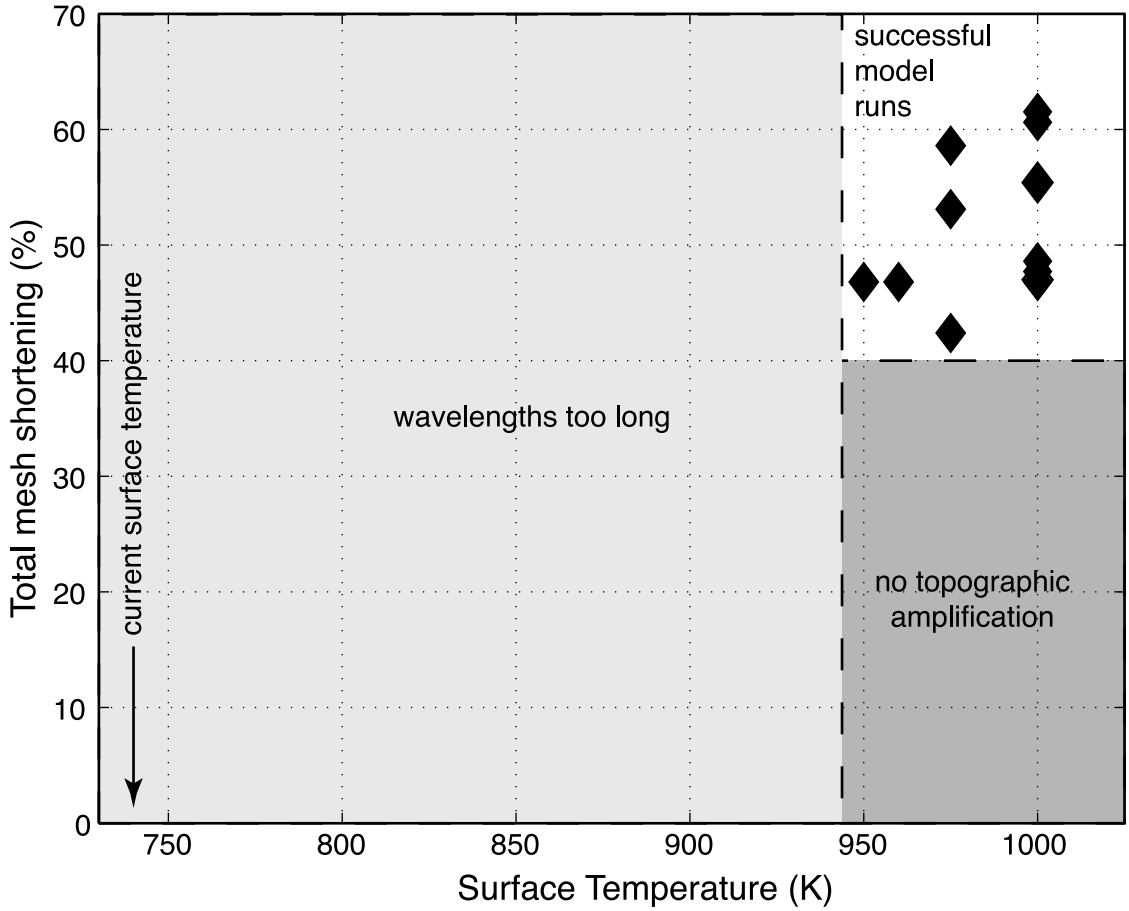


**Figure 9.** Plot showing locations of successful model runs in total shortening–surface temperature space. This plot illustrates the restricted range of parameters for which the desired results were obtained.

or (2) the rheology used in our models does not represent that of the real rocks. If the former is the case, and a lower surface temperature were used in similar simulations, it is probable that additional rheological domains dominated by brittle deformation would develop near the surface of the models, and creep would not play such a significant role at shallow depths. For the latter case, one possibility is that crustal plateaus are characterized by mechanically layered materials; in particular, if a mechanically strong layer were present in the shallow subsurface, a scenario like that treated in theoretical studies of folding and necking [e.g., *Fletcher*, 1974; *Smith*, 1979; *Fletcher and Hallet*, 1983] could pertain. In that case, the restriction on the surface temperature would no longer be needed, because development of the required rheological boundaries would not be thermally driven. However, the apparent absence of multiple spatially periodic extensional fabrics [*Ghent and Hansen*, 1999] argues against the presence of multiple mechanically distinct layers, unless additional regularly spaced extensional features exist unrecognized. Alternatively, we have seen that plasticity plays an important role in governing the aggregate behavior of the shallow part of each mesh, and it is possible that an alternate formulation for plasticity could produce different results, even under the high surface temperature conditions; however, an alternate plasticity criterion would not change the fact that a high surface temperature leads to the predominance of creep at all depths, inhibiting development of a purely brittle surface layer. As alluded to in section 4.1, this strong dominance of creep, and the resulting difficulty of forming folds of appreciable amplitude, render further exploration of numerical convergence issues by changing the plasticity criterion beyond the scope of this work. The general implications of including plasticity in such models, and the dependence of the results on the criterion used, are potentially interesting areas for further work.

[44] We conclude that the simplest resolution is that the high surface temperature requirement may not be appropriate. The constraint that crustal plateau surfaces seem to have been healed of previous structures prior to ribbon formation [*Hansen and Willis*, 1998] still supports local volumetric heating and resurfacing during the initial stages of crustal plateau deformation, consistent with their formation above mantle plumes. However, it is likely that the relationship between the wavelength progression of tectonic structures and changes in the thickness of the mechanical layer in which they formed is more complex than previously envisioned. If this is the case, it may be that both ribbons and short-wavelength folds formed simultaneously under more conventional thermal and mechanical conditions.

## 6. Conclusions

[45] On the basis of the results of our finite element modeling, we conclude that imposition of an elevated

surface temperature inhibits, rather than promotes, development of short-wavelength contractional structures with appreciable amplitude, because the effective integrated model strength under such hot conditions is too weak to readily develop finite amplitude folds. The thermal conditions produced by such a high surface temperature favor development in the finite element meshes of a near-surface semibrittle zone characterized by simultaneous small-scale, distributed faulting and microscopic creep rather than a surface brittle layer underlain by a sharp mechanical boundary that would promote significant structural amplification. Lowering the surface temperature in our simulations produces structures of larger amplitude but at wavelengths that are too large to match those observed. The inclusion of plasticity in the rheological model contributes to the formation of contractional features in this zone, but even modest topographic amplification requires an unrealistic degree of homogeneous shortening in the simulations. Though our results do not conflict with the notion that the surfaces of crustal plateaus appear to have been mechanically homogenized prior to the formation of the shortest-wavelength structures, they do suggest that a purely thermal control of mechanical properties cannot explain the formation of the short-wavelength contractional features observed in crustal plateaus.

[46] **Acknowledgments.** This work was supported in part by NASA grant NAG5-4562 to V.L.H. and Southern Methodist University. R.R.G. would like to thank Andrew Dombard for abundant help and fruitful discussions and for reviewing earlier versions of the ms, and Duncan Young for insightful dialog. The authors would also like to acknowledge a review by George Tuckwell, though he disagreed with our conclusions, and helpful comments from an anonymous reviewer.

## References

Albert, R. A., and R. J. Phillips (2000), Paleoflexure, *Geophys. Res. Lett.*, *27*, 2385–2388.

Albert, R. A., and R. J. Phillips (2002), Time-dependent effects in elasto-viscoplastic models of loaded lithosphere, *Geophys. J. Int.*, *151*, 612–621.

Albert, R. A., R. J. Phillips, A. J. Dombard, and C. D. Brown (2000), A test of the validity of yield strength envelopes with an elastoviscoplastic finite element model, *Geophys. J. Int.*, *140*, 399–409.

Banks, B. K., and V. L. Hansen (2000), Relative timing of crustal plateau magmatism and tectonism at Tellus, Regio, Venus, *J. Geophys. Res.*, *105*(E7), 17,655–17,667.

Barsukov, V. L., et al. (1986), The geology and geomorphology of the Venus surface as revealed by the radar images obtained Veneras 15 and 16, *Proc. Lunar Planet. Sci. Conf. 16th*, Part 2, *J. Geophys. Res.*, *91*, suppl., D378–D398.

Basilevsky, A. T., A. A. Pronin, L. B. Ronca, V. P. Kryuchkov, A. L. Sukhanov, and M. S. Markov (1986), Styles of tectonic deformation on Venus: Analysis of Venera 15 and 16 data, *Proc. Lunar Planet. Sci. Conf. 16th*, Part 2, *J. Geophys. Res.*, *91*, suppl., D399–D411.

Bindschadler, D. L. (1995), Magellan: A new view of Venus' geology and geophysics, *U.S. Natl. Rep. Int. Union Geod. Geophys. 1991–1994, Rev. Geophys.*, *33*, 459–467.

Bindschadler, D. L., and J. W. Head (1991), Tessera terrain, Venus: Characterization and models for origin and evolution, *J. Geophys. Res.*, *96*, 5889–5907.

Bindschadler, D. L., G. Schubert, and W. M. Kaula (1992a), Coldspots and hotspots: Global tectonics and mantle dynamics of Venus, *J. Geophys. Res.*, *97*, 13,495–13,532.

Bindschadler, D. L., A. deCharon, K. K. Beratan, S. E. Smrekar, and J. W. Head (1992b), Magellan observations of Alpha Regio: Implications for formation of complex ridged terrains on Venus, *J. Geophys. Res.*, *97*, 13,563–13,577.

Biot, M. A. (1961), Theory of folding of stratified viscoelastic media and its implications in tectonics and orogenesis, *Geol. Soc. Am. Bull.*, *72*, 1595–1620.

Brown, C. D., and R. E. Grimm (1997), Tessera deformation and the contemporaneous thermal state of the plateau highlands, Venus, *Earth Planet. Sci. Lett.*, *147*, 1–10.

Brown, C. D., and R. J. Phillips (2000), Crust-mantle decoupling by flexure on continental lithosphere, *J. Geophys. Res.*, *105*, 13,221–13,237.

Bullock, M. A., and D. H. Grinspoon (2001), The recent evolution of climate on Venus, *Icarus*, *150*, 19–37.

Dombard, A. J., and A. M. Freed (2002), Thermally induced lineations on the asteroid Eros: Evidence of orbit transfer, *Geophys. Res. Lett.*, *29*(16), 1818, doi:10.1029/2002GL015181.

Dombard, A. J., and W. B. McKinnon (2000), Long-term retention of impact crater topography on Ganymede, *Geophys. Res. Lett.*, *27*, 3663–3666.

Fletcher, R. C. (1974), Wavelength selection in the folding of a single layer with power-law rheology, *Am. J. Sci.*, *274*, 1024–1043.

Fletcher, R. C., and B. Hallet (1983), Unstable extension of the lithosphere: A mechanical model for Basin-and-Range structure, *J. Geophys. Res.*, *88*(B9), 7457–7466.

Ghent, R. R., and V. L. Hansen (1999), Structural and kinematic analysis of eastern Ovda Regio, Venus: Implications for crustal plateau formation, *Icarus*, *139*, 116–136.

Ghent, R. R., and I. M. Tibuleac (2002), Ribbon spacing in Venusian tessera: Implications for layer thickness and thermal state, *Geophys. Res. Lett.*, *29*(20), 2000, doi:10.1029/2002GL015994.

Gilmore, M. S., M. A. Ivanov, J. W. Head, and A. T. Basilevsky (1997), Duration of tessera deformation on Venus, *J. Geophys. Res.*, *102*, 13,357–13,368.

Gilmore, M. S., G. C. Collins, M. A. Ivanov, L. Marinangeli, and J. W. Head (1998), Style and sequence of extensional structures in tessera terrain, Venus, *J. Geophys. Res.*, *103*, 16,813–16,840.

Grimm, R. E. (1994), The deep structure of Venusian plateau highlands, *Icarus*, *112*, 89–103.

Hansen, V. L., and J. J. Willis (1996), Structural analysis of a sampling of tesserae: Implications for Venus geodynamics, *Icarus*, *123*, 296–312.

Hansen, V. L., and J. J. Willis (1998), Ribbon terrain formation, southwestern Fortuna Tessera, Venus: Implications for lithosphere evolution, *Icarus*, *132*, 321–343.

Hansen, V. L., J. J. Willis, and W. B. Banerdt (1997), Tectonic overview and synthesis, in *Venus II: Geology, Geophysics, Atmosphere, and Solar Wind Environment*, edited by S. W. Bougher et al., pp. 797–844, Univ. of Ariz. Press, Tucson.

Hansen, V. L., B. K. Banks, and R. R. Ghent (1999), Tessera terrain and crustal plateaus, Venus, *Geology*, *27*, 1071–1074.

Hansen, V. L., R. J. Phillips, J. J. Willis, and R. R. Ghent (2000), Structures in tessera terrain: Issues and answers, *J. Geophys. Res.*, *105*(E2), 4135–4152.

Head, J. W., and A. T. Basilevsky (1998), Sequence of tectonic deformation in the history of Venus: Evidence from global stratigraphic relationships, *Geology*, *26*, 35–38.

Head, J. W., and L. S. Crumpler (1987), Evidence for divergent plate-boundary characteristics and crustal spreading on Venus, *Science*, *288*, 1380–1385.

Herrick, R. R., and R. J. Phillips (1990), Blob tectonics: A prediction for western Aphrodite Terra, Venus, *Geophys. Res. Lett.*, *17*(12), 2129–2132.

Hofmeister, A. (1999), Mantle values of thermal conductivity and the geotherm from phonon lifetimes, *Science*, *283*, 1699–1706.

Ivanov, M. A., and J. W. Head (1996), Tessera terrain on Venus: A survey of the global distribution, characteristics, and relation to surrounding units from Magellan data, *J. Geophys. Res.*, *101*, 14,861–14,908.

Kidder, J. G., and R. J. Phillips (1996), Convection-driven subsolidus crustal thickening on Venus, *J. Geophys. Res.*, *101*, 23,181–23,294.

Kohlstedt, D. L., B. Evans, and S. J. Mackwell (1995), Strength of the lithosphere: Constraints imposed by laboratory experiments, *J. Geophys. Res.*, *100*(B9), 17,587–17,602.

Mackwell, S. J., M. E. Zimmerman, and D. L. Kohlstedt (1998), High-temperature deformation of dry diabase with application to tectonics on Venus, *J. Geophys. Res.*, *103*, 975–984.

Mancktelow, N. S. (1999), Finite-element modelling of single-layer folding in elasto-viscous materials: The effect of initial perturbation geometry, *J. Struct. Geol.*, *21*, 161–177.

Montési, L. G. J., and M. T. Zuber (2002), A unified description of localization for application to large-scale tectonics, *J. Geophys. Res.*, *107*(B3), 2045, doi:10.1029/2001JB000465.

Montési, L. G. J., and M. T. Zuber (2003), Spacing of faults at the scale of the lithosphere and localization instability: 1. Theory, *J. Geophys. Res.*, *108*(B2), 2110, doi:10.1029/2002JB001923.

Nunes, D. C., R. J. Phillips, C. D. Brown, and A. J. Dombard (2004), Relaxation of compensated topography and the evolution of crustal

plateaus on Venus, *J. Geophys. Res.*, *109*, E01006, doi:10.1029/2003JE002119.
Phillips, R. J. (1986), A mechanism for tectonic deformation on Venus, *Geophys. Res. Lett.*, *13*, 1141–1144.
Phillips, R. J. (1990), Convection-driven tectonics on Venus, *J. Geophys. Res.*, *95*(B2), 1301–1316.
Phillips, R. J., and V. L. Hansen (1994), Tectonic and magmatic evolution of Venus, *Annu. Rev. Earth Planet. Sci.*, *22*, 597–656.
Phillips, R. J., and V. L. Hansen (1998), Geological evolution of Venus: A geodynamical and magmatic framework, *Science*, *279*, 1492–1497.
Phillips, R. J., R. E. Grimm, and M. C. Malin (1991), Hot-spot evolution and the global tectonics of Venus, *Science*, *252*, 651–658.
Phillips, R. J., M. A. Bullock, and S. A. Hauck II (2001), Climate and interior coupled evolution on Venus, *Geophys. Res. Lett.*, *28*, 1779–1782.
Pritchard, M. E., V. L. Hansen, and J. J. Willis (1997), Structural evolution of western Fortuna Tessera, Venus, *Geophys. Res. Lett.*, *24*, 2339–2342.
Ramberg, H. (1962), Contact strain and folding instability of a multilayered body under compression, *Geol. Rundsch.*, *51*, 405–439.
Scargle, J. D. (1982), Studies in astronomical time series analysis. II. Statistical aspects of spectral analysis of unevenly spaced data, *Astrophys. J.*, *263*, 835–853.
Scargle, J. D. (1989), Studies in astronomical time series analysis. III. Fourier transforms, autocorrelation functions, and cross-correlation functions of unevenly spaced data, *Astrophys. J.*, *343*, 874–887.
Schulz, M., and K. Stattegger (1997), Spectrum: Spectrum analysis of unevenly spaced paleoclimatic time series, *Comput. Geosci.*, *23*, 929–945.
Sherwin, J., and W. M. Chapple (1968), Wavelengths of single layer folds: A comparison between theory and observation, *Am. J. Sci.*, *266*, 167–179.
Smith, R. B. (1977), Formation of folds, boudinage and mullions in non-Newtonian materials, *Geol. Soc. Am. Bull.*, *88*, 312–320.
Smith, R. B. (1979), The folding of a strongly non-Newtonian layer, *Am. J. Sci.*, *279*, 272–287.
Smrekar, S. E., and R. J. Phillips (1991), Venusian highlands: Geoid to topography ratios and their implications, *Earth Planet. Sci. Lett.*, *107*, 582–597.
Turcotte, D. L., and G. Schubert (1982), *Geodynamics: Application of Continuum Physics to Geological Problems*, John Wiley, Hoboken, N. J.
Zhang, Y., B. E. Hobbs, A. Ord, and H. B. Mühlhaus (1996), Computer simulation of single-layer buckling, *J. Struct. Geol.*, *18*, 643–655.
Zhang, Y., N. S. Mancktelow, B. E. Hobbs, A. Ord, and H. B. Mühlhaus (2000), Numerical modelling of single-layer folding: Clarification of an issue regarding the possible effect of computer codes and the influence of initial irregularities, *J. Struct. Geol.*, *22*, 1511–1522.
Zuber, M. T., and E. M. Parmentier (1996), Finite amplitude folding of a continuously viscosity-stratified lithosphere, *J. Geophys. Res.*, *101*(B3), 5489–5498.

R. R. Ghent, Center for Earth and Planetary Studies, Smithsonian Institution, P.O. Box 37012, NASM Room 3754, Washington, DC 20013, USA. (ghentr@si.edu)

V. L. Hansen, Department of Geological Sciences, University of Minnesota, 231 Heller Hall, 1114 Kirby Drive, Duluth, MN 55812, USA.

D. C. Nunes, Lunar and Planetary Institute, 3600 Bay Area Boulevard, Houston, TX 77058, USA.

R. J. Phillips, Department of Earth and Planetary Sciences, Washington University, Campus Box 1169, 1 Brookings Drive, St. Louis, MO 63130, USA.